

Bright correlated photon pairs based on double-lambda scheme in a cold atomic ensemble

Yifan Li, Chang Hoong Chow, Boon Long Ng, and Vindhiya Prakash

Centre for Quantum Technologies, National University of Singapore, 3 Science Drive 2, Singapore 117543

Christian Kurtsiefer

Centre for Quantum Technologies, National University of Singapore, 3 Science Drive 2, Singapore 117543 and

*Department of Physics, National University of Singapore, 2 Science Drive 3, Singapore 117551**

We demonstrate a bright narrowband correlated photon-pair source using the double- Λ four-wave mixing in a cold atomic ^{87}Rb ensemble. The time-frequency-correlated photon pairs are generated in the twin Stokes and anti-Stokes modes in the presence of two pump fields. We have determined that the correlated photon pair generation rate can reach 10^6 per second within a spatial mode with a waist of $175\ \mu\text{m}$ in the paraxial region. By investigating the influence of pump field intensity, detuning, and atomic cloud optical depth, we have characterized the properties of this photon pair source. These findings highlight the need for further theoretical development to fully comprehend the distinct properties exhibited by these correlated photon pairs.

I. INTRODUCTION

Correlated photons constitute a valuable quantum resource with diverse applications, particularly within the domains of quantum communication [1, 2], quantum computation [3] and quantum metrology [4]. Correlated photon pairs are conventionally generated through spontaneous parametric downconversion (SPDC) processes in nonlinear crystals [5, 6] or spontaneous four-wave mixing (FWM) in atomic media comprising both hot atomic gases [7–9] and cold atomic ensembles [10–12]. In contrast to SPDC, temporally correlated photon pairs derived from cold atomic ensembles exhibit narrow bandwidth characteristics inherited from the intrinsic atomic natural linewidth. This property makes them favorable for direct interactions with atoms. Moreover, these photon pairs possess an adjustable coherence time [13–15], thereby offering potential advantages for long-distance quantum communication. The parametric FWM process can resort to various energy level configurations, an approach relies on cascaded emission originating from cascade-shaped energy levels [12, 16, 17]. The alternative protocols employ the double- Λ scheme [18–20] to generate correlated photon pairs. The existence of electromagnetically-induced transparency (EIT) [21] within one of the Λ energy levels benefits the photon pair generation, as it can establish a spectrally transparent window that significantly reduces the absorption loss of resonant photons traveling through the atomic ensemble. Furthermore, the slow light effect induced by EIT allows for the modulation of the coherence time of correlated photon pairs [13, 22]. A series of theoretical investigations [20, 23–25] has emerged to describe the two-photon wave function of correlated photon pairs from such SFWM. These studies systematically categorize two-photon wave functions in both the oscillation

regime and the group delay regime, which are consistent with experimental observations [18, 22, 26, 27].

In this work, we present a bright correlated photon source from a ^{87}Rb cold atomic ensemble based on the double- Λ four-wave mixing parametric process. This source is implemented within the paraxial regime ($\sim 1^\circ$) of continuous-wave pump fields within a small collective spatial mode of $175\ \mu\text{m}$ waist. We recorded a high pair generation rate, which is compatible with the previous correlated photon pair source in the cascaded FWM protocol [17] and in a similar double- Λ scheme [28]. Considering the geometric symmetry of our counterpropagating pump configurations, small collection solid angle, and the subpar performance of the spectral filter systems used in our experimental setup, it is reasonable to anticipate a higher photon pair generation rate by optimizing the collection setup and improving filter efficiencies. In our experiment, we observed distinct properties in the characteristics of the correlated photon pair source. These features, such as a fast decay envelope in the two-photon wave function and dependencies on optical depth (OD), can be tentatively attributed to collective emission effects, also known as superradiance [29, 30]. Some analogous collective behaviors have also been reported in the nonlinear process in the atomic ensemble, such as the “read” process of the Duan-Lukin-Cirac-Zoller (DLCZ) protocol [10, 31] and the parametric process within cascaded four-wave mixing [12, 16, 32–34].

This paper is structured as follows. Sec.II details the experimental protocol and setup for measuring the time-correlated photon pairs. Sec.III reviews theoretical interpretations for the two-photon wave function based on existing theoretical results and represents an example of photon pair characteristics under specific parameters. Then in Sec.V, Sec.VI, and Sec.VII, we characterize the correlated photon pair source with respect to pump field intensity, optical depth (OD), and pump field detuning, respectively, within certain experimental parameter ranges. Finally, we summarize in Sec.VIII.

* christian.kurtsiefer@gmail.com

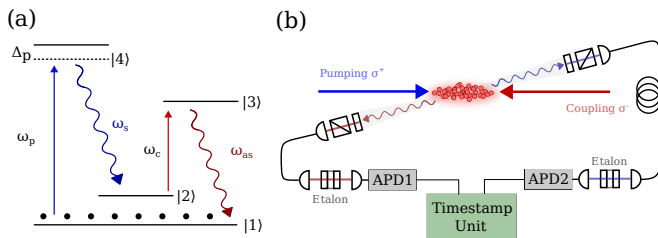


FIG. 1. (a) The double- Λ atomic energy levels involved in the four-wave mixing process. (b) Schematic representation of the experimental setup. The pumping beam and coupling beam counterpropagate along the longest axis of a cigar-shaped atomic ensemble, with a collection path angled by approximately 1 degrees.

II. EXPERIMENTAL SETUP

The experimental protocol involves double- Λ atomic energy levels driven by the “pumping” field and the “coupling” field, denoted as ω_p and ω_c , respectively. As shown in Fig.1 (a), the pumping laser is detuned by Δ_p from the $|5S_{1/2}, F = 1\rangle \leftrightarrow |5P_{3/2}, F = 2\rangle$ transition and the coupling laser is initially resonant to the $|5S_{1/2}, F = 2\rangle \leftrightarrow |5P_{1/2}, F = 2\rangle$ transition with $\Delta_c = 0$. The pumping field is right circularly polarized (σ^+) while the coupling field is left circularly polarized (σ^-). In the experimental setup, depicted in Fig.1 (b), a backward-propagation configuration is implemented, wherein the coupling beam and pumping beam with a waist of roughly $850 \mu\text{m}$ counter-propagate collinearly. This arrangement minimizes residual Doppler effects and facilitates spatial discrimination of the generated photons from the pump fields. The experimental setup employs an elongated cloud of ^{87}Rb atoms, with a length of approximately 5 mm and a transverse cross section of $2 \times 4 \text{ mm}$. The control sequence consists of a 10 ms cooling stage followed by a $400 \mu\text{s}$ state transfer stage and a 1 ms measurement stage. After the state preparation, the majority of atoms are prepared in the $|5S_{1/2}, F = 1\rangle$ state.

The collection path diverges from the pumping and coupling beam by a small angle of roughly 1 degree with a focused Gaussian mode with an estimated waist of around $175 \mu\text{m}$, which spatially overlaps with the pump area in the atomic ensemble. This configuration corresponds to a collection volume of approximately $5 \times 10^{-4} \text{ cm}^3$. Before coupling into the single-mode fibers, the collected photons are filtered by polarization filters consisting of a quatre-wave plate and a polarizing beam splitter. The angles of quatre-wave plates are chosen to maximize the photon pair rate. Subsequently, the collected photons undergo spectral filterings via temperature-controlled fused-silica Etalons. These filters serve to eliminate scattering photons from the pump fields and transmit photons centered at target frequencies ω_s and ω_{as} . The Etalon for Stokes photon has a bandwidth of 275 MHz and an extinction ratio of 34 dB

at the pumping frequency. Conversely, the Etalon for the anti-Stokes photon displays a bandwidth of 345 MHz and an extinction ratio of 40 dB at the control field frequency. The total collection efficiencies (total transmission ratio) are characterized as around 17% for Stokes photons and 16% for anti-Stokes photons. In our measurement setup, we use two Excelitas single-photon detectors. These detectors have expected detection efficiencies of approximately 70% for the Stokes channel and 50% for the anti-Stokes channel. To measure auto-correlation functions, we modify the setup to include a 50:50 fiber beam splitter. This splitter directs the light into two paths, each leading to a single-photon detector. The photon event signals from these detectors are then recorded using a timestamp card with a timing resolution of 2 ns.

III. TWO-PHOTON WAVE FUNCTION

The correlated photon pairs from this FWM process have been theoretically modeled using the Heisenberg-Langevin method [24, 25] and perturbation theory [13, 20]. The perturbation theory method provides a macroscopic interpretation of the correlated pair generation mechanism in the nonlinear process, neglecting the effect of the higher terms of the Hamiltonian. For the sake of simplicity, here we present the theoretical result using perturbation theory [20]. The biphoton function $\Psi(\tau = t_{as} - t_s)$ between correlated Stokes and anti-Stokes photons is a convolution of the nonlinear response $\tilde{\kappa}(\tau)$ and the phase matching $\tilde{\Phi}(\tau)$ in the time domain as

$$\Psi(\tau) = \tilde{\kappa}(\tau) \star \tilde{\Phi}(\tau). \quad (1)$$

These two functions are the Fourier transform of nonlinear coupling coefficient $\kappa(\omega_{as})$ and longitudinal detuning function $\Phi(\omega_{as})$ in the frequency domain as

$$\begin{aligned} \Psi(\tau) &= \frac{L}{2\pi} \int d\omega_{as} \kappa(\omega_{as}) \Phi(\omega_{as}) e^{-\omega_{as}\tau}, \\ \Phi(\omega_{as}) &= \text{sinc}\left(\frac{\Delta k L}{2}\right) e^{i(k_{as} + k_s)L/2}, \\ \kappa(\omega_{as}) &= \frac{-i\sqrt{\omega_{as}\omega_s}}{2} \chi^{(3)} E_p E_c, \end{aligned} \quad (2)$$

where $\Delta k = (\vec{k}_{as} + \vec{k}_s) - (\vec{k}_p + \vec{k}_c)$ is the phase mismatching. $\kappa(\omega_{as})$ represents the effect of third-order nonlinear susceptibility $\chi^{(3)}$ in the double- Λ atomic energy levels, while $\Phi(\omega_{as})$ denotes the phase-matching bandwidth, which will be affected by the linear susceptibility in atomic media. The nonlinear coupling coefficient predicts two resonances separated by effective coupling Rabi frequency Ω_e in the atomic spectrum. The effective coupling Rabi frequency is defined as $\Omega_e = \sqrt{|\Omega_c|^2 - (\gamma_{13} - \gamma_{12})^2}$, where γ_{12} is the dephasing rate of $|1\rangle \leftrightarrow |2\rangle$ and γ_{13} is the decay rate of $|1\rangle \leftrightarrow |3\rangle$. These resonances have a linewidth of $2\gamma_e = (\gamma_{12} + \gamma_{13})/2$. Additionally, the linear susceptibilities χ_s and χ_{as} vary the dispersion relations

of the generated photons in the atomic media. Resonant coupling field Ω_c generates a transparency EIT window for the anti-Stokes photons and modulates its group velocity due to the slow-light effect. Therefore, depending on which spectrum dominates, such correlated photon pair source is classified into the damped Rabi oscillation regime and the group delay regime. When the group delay time $\tau_g = L/v_g \approx (2\gamma_{13}/|\Omega_c|^2)\text{OD}$ is smaller than the coherence time $\tau_e = 1/\gamma_e$, the phase-matching bandwidth is constant as $\Phi(\omega) = 1$. The two-photon wave function is determined by the nonlinear coupling function as

$$\begin{aligned} \tilde{\kappa}(\tau) &= B e^{-\gamma_e \tau} \sin\left(\frac{\Omega_e \tau}{2}\right) \Theta(\tau) e^{-i\omega_{as}\tau}, \\ B &= -i \frac{N \mu_{13} \mu_{32} \mu_{24} \mu_{41} \sqrt{\omega_{as} \omega_s}}{4c \varepsilon_0 \hbar^3 \Omega_e (\Delta_p + i\gamma_{14})}. \end{aligned} \quad (3)$$

Here, $\Theta(\tau)$ is the step function starting from $\tau = 0$, B represents the nonlinear strength, N denotes the number of atoms, μ_{jk} denotes the dipole moment for the atomic transition from states $|j\rangle$ to $|k\rangle$, and γ_{jk} represents the decay rate for corresponding atomic transition. When the group delay time is larger than the coherence time τ_e , the group-delay bandwidth dominates in the biphoton spectrum as

$$\Phi(\omega) \simeq \text{sinc}\left(\frac{\omega L}{2V_g} + i\frac{\alpha L}{2}\right) \exp\left(i\frac{\omega L}{2V_g} - \frac{\alpha L}{2}\right), \quad (4)$$

where α represents the EIT loss and V_g denotes the group velocity for anti-Stokes photon. This phase-matching bandwidth leads to a rectangle function delayed by τ_g group delay function in $\tilde{\Phi}(\tau)$ in the time domain.

IV. CROSS-CORRELATION

A. Normalized cross-correlation function

The two-photon wave function $\Psi(\tau)$ determines the Glauber's second-order correlation function between Stokes and anti-Stokes photons as

$$\begin{aligned} G_{\text{as-s}}^{(2)}(\tau) &= \langle \hat{a}_s^\dagger(\tau) \hat{a}_{as}^\dagger(t+\tau) \hat{a}_{as}(t+\tau) \hat{a}_s(t) \rangle \\ &= |\Psi(\tau)|^2 + R_s R_{as}, \end{aligned} \quad (5)$$

where R_s and R_{as} denote the single photon rate in Stokes and anti-Stokes channels respectively. This cross-correlation function can be obtained from the photon coincidence counting between twin modes. Furthermore, the normalized cross-section function is given as

$$g_{\text{as-s}}^{(2)}(\tau) = \frac{G_{\text{as-s}}^{(2)}(\tau)}{R_s R_{as}}. \quad (6)$$

This function signifies the strong time correlation for twin photons as a Stokes photon precedes the presence of an anti-Stokes photon within the coherence time. Fig.2

(a)-(d) illustrates the normalized cross-correlation functions $g_{\text{as-s}}^{(2)}(\tau)$ corrected by the accidental background caused by the imperfections in the collection and detection setup (refer to Appendix.B). In the damped Rabi oscillation regime, the theories reviewed in Sec.III predict the cross-correlation function $g_{\text{as-s}}^{(2)}(\tau)$ has a decay envelope as $e^{-\Gamma_e \tau} \simeq e^{-2\gamma_{13}\tau}$. However, in an example shown in Fig.2 (a), the waveform of $g_{\text{as-s}}^{(2)}(\tau)$ is characterized by a distinct decay envelope feature with an enhanced decay rate as $\Gamma_e \simeq 3.1\Gamma$. Conversely, the experimental parameters corresponding to Fig.2 (d) predict a group delay about $\tau_g \simeq 91$ ns for the propagation of anti-Stokes photon in a $\text{OD} = 30$ atomic ensemble. While it is anticipated that the waveform would be delayed, but the observed waveform does not match the expected time convolution of this group delay time.

B. Coincidence count and pair detection

In this section, we exemplify the characteristics of correlated photon pairs measured under specific experimental conditions. These conditions were chosen to balance the trade-off between photon pair rate and noise, rather than simply maximizing the pair rate. Furthermore, the initial state of the photon state is inferred by accounting for the effects of transmission ratios and detection efficiencies within our experimental setup.

Under the experimental pumping field powers as $P_p \simeq 300 \mu\text{W}$, $P_c \simeq 8.5 \text{ mW}$, and field detuning settings as $\Delta_p = +25 \text{ MHz}$ and $\Delta_c = 0$, we record Stokes photons at an instantaneous rate of $(5.1 \pm 0.2) \times 10^5 \text{ s}^{-1}$, and anti-Stokes photons at the rate of $(6.1 \pm 0.2) \times 10^5 \text{ s}^{-1}$. Within a coincidence window of 22 ns, the measured correlated photon pair rate R_p^m , defined as the average detection rate of correlated photons during the measurement time, is $(2.05 \pm 0.07) \times 10^4 \text{ s}^{-1}$, with heralding efficiency 4.0% for Stokes channel and 3.3% for anti-Stokes. The correlated-to-accidental ratio (CAR) is measured at around 3 within this coincidence window. Typically, the quantum properties of correlated photon pairs are confirmed by demonstrating the violation of the Cauchy-Schwarz inequality:

$$(g_{\text{as-s}}^{(2)}(\tau))^2 / g_{\text{as}}^{(2)}(\tau) g_s^{(2)}(\tau) \leq 1. \quad (7)$$

For Stokes and anti-Stokes photons, the auto-correlation functions at zero-delay are given as $g_{\text{s-s}}^{(2)}(0) = 1.95 \pm 0.12$ and $g_{\text{as-as}}^{(2)}(0) = 1.99 \pm 0.11$, indicating residual thermal statistics in one mode after tracing out the twinned mode. Therefore, the violation of the Cauchy-Schwarz inequality is related to the normalized cross-correlation peak as $g_{\text{as-s}}^{(2)}$. $g_{\text{as-s}}^{(2)}$ has a measured maximum of (7.5 ± 0.1) , indicating that it violates the Cauchy-Schwarz inequality by a factor of 14.

One of the noise sources in photon coincidence counting measurements arises from optical losses in the subpar

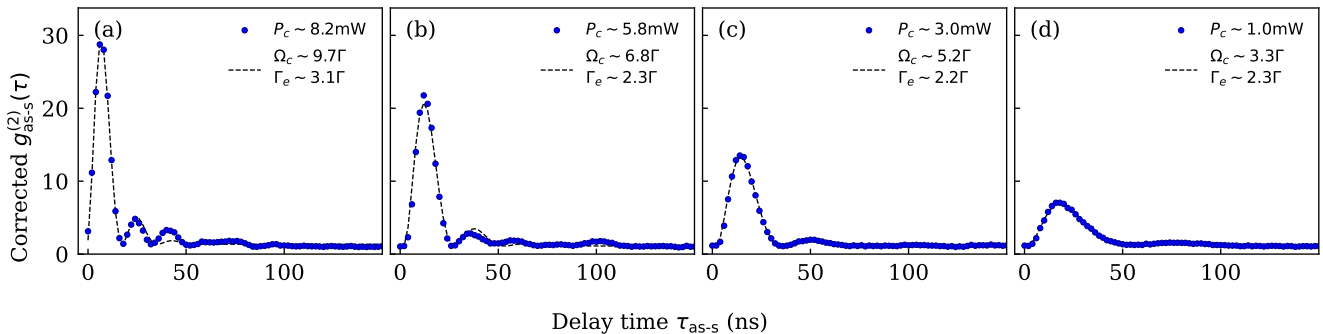


FIG. 2. (a)-(d) illustrate the corrected normalized cross-correlation function $g_{as-s}^{(2)}(\tau)$ under different power of coupling beams with the same power of pumping beams $P_p \simeq 500 \mu\text{W}$ and $\text{OD} = 30$. The dashed lines are corresponding fits using the waveform model as $\exp(-\Gamma_e t)(1 - \cos(\Omega_e \tau))\Theta(\tau)$ from the two-photon wave function in the damped oscillation regime. The fitted Rabi frequencies Ω_e and effective decay rate Γ_e are denoted in terms of the natural linewidth of $|5P_{1/2}, F = 2\rangle$ as $\Gamma = 2\pi \times 5.746 \text{ MHz}$. The correction is performed using the transmission values $\eta_s = 0.17$, $\eta_{as} = 0.16$, and detection efficiencies $\eta_{d-s} = 70\%$, $\eta_{d-as} = 50\%$.

collection and filtering system, resulting in expected total transmission ratios of $\eta_t^s \simeq 0.17$ for Stokes channels and $\eta_t^{as} \simeq 0.16$ for the anti-Stokes channel. By inclusively accounting for these losses and the detection efficiencies of single-photon detectors, we can correct the noise caused by these imperfections in the collection and measurement devices. This allows us to infer the initial photon state within the same spatial modes. Using the relation $R_p = R_p^m / (\eta_s \eta_{as})$, the initial photon state has a pair rate of around $2.5 \times 10^6 \text{ s}^{-1}$. The heralding efficiencies are about 58% for the Stokes channel and 32% for anti-Stokes channels. Based on the corrected normalized cross-correlation function, we anticipate that the Cauchy-Schwarz inequality is violated by a factor of 65. This correction for cross-correlation refers to the method detailed in Appendix.B which corrects the contributions from dark counts, laser leakage, and unpaired photons in accidental coincidence counting background. Among these, the accidental photon counts, attributed to the dark counts of detectors and laser leakages are evaluated as $R_s^d \simeq 5300 \text{ s}^{-1}$ for Stokes channel, and $R_{as}^d \simeq 3100 \text{ s}^{-1}$ for anti-Stokes channel.

V. PUMP INTENSITY DEPENDENCE

Conventionally, we use laser power to represent the corresponding field intensity levels. The pump field intensities affect the two-photon wave function and the strength of the nonlinear process, as indicated by Eq.3. Additionally, the pump field intensities also influence the phase-matching condition and the propagation of correlated photon pairs through linear susceptibility, whereby the group velocity is modulated in the atomic medium as described in Eq.4. Fig.3 (a) illustrates that the correlated photon pair mechanism operates at both negative and positive detuning sides of the energy level $|5P_{3/2}, F = 2\rangle$. At a specific detuning, as the pump-

ing field power increases, the correlated photon pair rate initially rises and then saturates. Further increases in the pumping field power cannot significantly enhance the photon pair rate; instead, they lead to an increase in the single-photon rates $R_{s/as}$, due to the incoherent scattering photons. Consequently, the increased noise photons reduce the heralding efficiencies in both modes, as shown in Fig.3 (c) and (d), and increase the accidental photon pair rate $R_s R_{as} t_{\text{coi}}$, defined within a coincidence window t_{coi} . The $g_{as-s}^{(2)}$ maximum value and CAR in Fig.4 also suggest that the increases of the pumping field power undermine the quantum features by reducing the violation factor of Cauchy-Schwarz inequality and minimize the purity of the obtained correlated photon pairs.

When varying the power of the coupling beam within the range of 1 mW to 8.5 mW for different settings of pumping field power. Fig.5 suggests that correlated photon pair rate saturates once the coupling field power reaches a certain threshold. The heralding efficiency in the Stokes channel benefits from this increase, while the anti-Stokes heralding efficiency suffers due to increased incoherent scattering photon. Fig.2 (a)-(d) also depict the evolution of cross-correlation functions with varying coupling field power. As the coupling field power increases, the total correlated photon pair rate remains roughly unchanged, while the coherence time becomes narrow, corresponding to the increase of $g_{as-s}^{(2)}$ maximum in Fig.5 (d).

The bandwidth observations depicted in Fig.6 demonstrate a consistent linear relationship between the spectral bandwidth and the coupling field power. As the coupling field power increases, the bandwidths vary from sub-natural linewidth to an enhanced bandwidth that is broader than the natural linewidth. When the power of the coupling beam is kept constant, the spectral bandwidths remain stable, irrespective of the pumping field power. This dependence on the coupling field power follows a similar trend to the theoretical prediction of

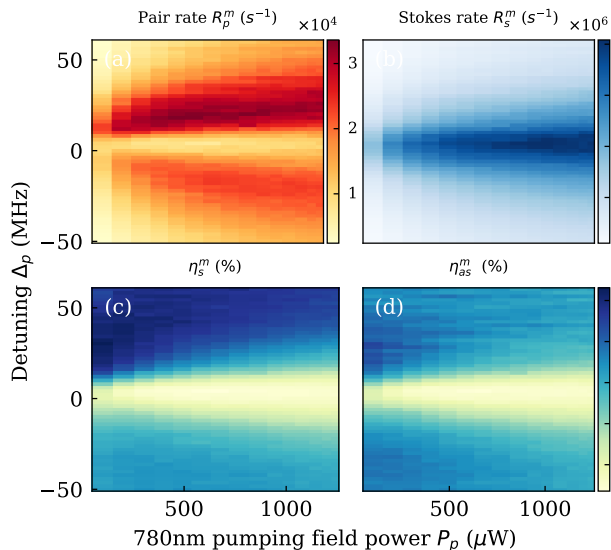


FIG. 3. Panels (a)-(b) show the characteristics as joint functions of the pumping field power and its detuning, using a resonant coupling field with a power of $P_c \simeq 8.5$ mW. The characteristics displayed are (a) the correlated photon pair rate, (b) the single photon detection rate in the Stokes channel, (c) the heralding efficiency for Stokes photons, and (d) the heralding efficiency for anti-Stokes photons.

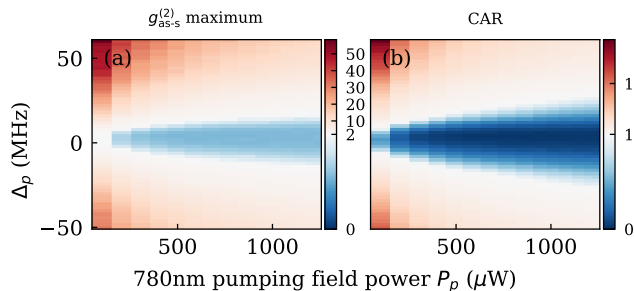


FIG. 4. (a) The $g_{as-s}^{(2)}$ maximum value, only corrected by dark counts. (b) CAR within a coincidence window of 22 ns, corresponding to the dominant peak in the cross-correlation function.

the group delay bandwidth, given by $\Delta\omega_g \simeq 0.88/\tau_g$, where the group delay time τ_g is characterized by $\tau_g \simeq 2\gamma_{13}OD/|\Omega_c|^2$.

VI. OPTICAL DEPTH DEPENDENCE

Optical depth (OD) provides an alternative representation for the number of atoms involved, as it is directly proportional to the atom number within the interaction volume. It is defined as $OD = n\sigma L$, where n is the atomic density, σ represents the cross-section and L indicates the length of the atomic ensemble (volume length). Some theoretical investigations [20] predict that the correlated photon pair rate and the atom number follow a

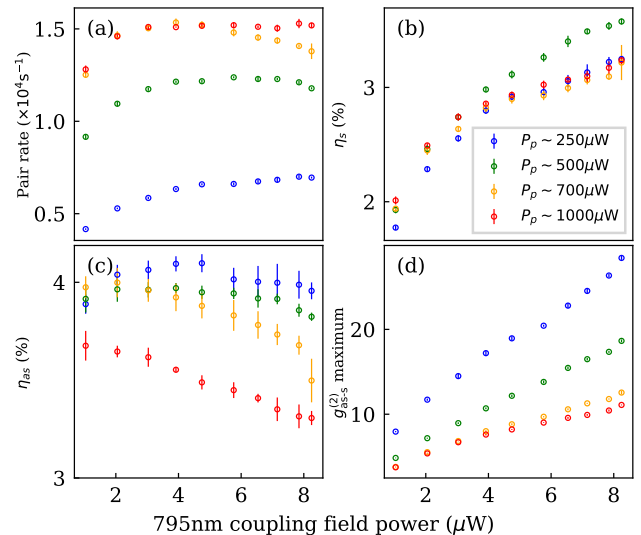


FIG. 5. Figures (a)-(d) illustrate the correlated photon pair rate, heralding efficiency in Stokes channels, heralding efficiency in anti-Stokes channel, and the maximum value of $g_{as-s}^{(2)}$ as functions of coupling field power under varying pumping field powers.

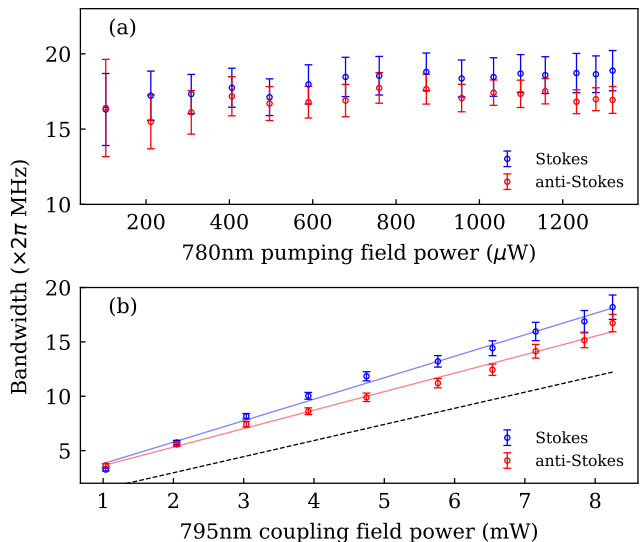


FIG. 6. Figure (a) illustrates the bandwidth as a function of pumping field power, while maintaining the coupling field power at a constant level of 8.5 mW. Figure (b) displays the bandwidths with respect to the coupling field power. The solid lines are linear fits for the data while the dashed black line represents the theoretical group-delay bandwidth $\Delta\omega_g$ with parameters $\gamma_{13} = 2\pi \times 3$ MHz, $OD = 30$. These bandwidths are fitted from the respective auto-correlation coincidence measurements.

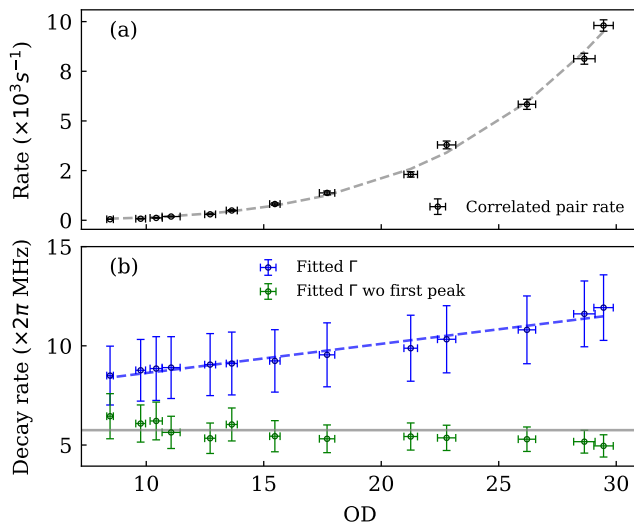


FIG. 7. Figure (a) illustrates the relationship between correlated photon pairs and optical depth (OD), with a dashed line depicting a fitted curve proportional to OD^4 . In Figure (b), the decay rate is derived from two-photon cross-correlation functions. For oscillations excluding the initial peak, the decay rate (green plot) closely aligns with the natural linewidth, while when considering the first oscillation, an OD dependence in the decay rate occurs. The red dashed line is fitted to the data using the model $\Gamma_0(1 + \alpha OD)$. The OD is measured by fitting the transmission profile at various detuning frequencies of the weak probe light. Following a cooling stage, the initial optical depth for the $|F = 2\rangle$ hyperfine state can reach approximately 80. Subsequently, after the transfer stage to the $|F = 1\rangle$ hyperfine state, the remaining maximal OD for this ground state is measured at around 30.

quadratic relation in the damped Rabi oscillation regime of a double- Λ FWM process. Fig.7 illustrates the characteristics of correlated photon pair rate within a 22 ns coincidence window with respect to OD, showing that the photon pair rate scales faster than the quadratically. This scaling can be interpreted as a result of superradiance, where the superradiant emission intensity scales quadratically with the number of atoms. Considering the contribution of this effect, the correlated photon pair rate is proportional to the fourth power of the optical depth (OD). The fit with OD^4 in Fig.7 (a) shows good agreement with the measured data, thereby supporting this superradiance interpretation to a certain degree.

We have observed that the two-photon wave function exhibits a decay envelope with an enhanced decay rate compared to the natural linewidth Γ_0 in the damped Rabi oscillation regime, as illustrated in Fig.2. We investigate these decay rates, fitted from the normalized cross-correlation function $g_{as-s}^{(2)}(\tau)$ as a function of the OD in Fig.7 (b). The fitted decay rates derived from the residual oscillations, excluding the first peak, remain constant around the Γ_0 even as the OD varies. In contrast, the fitted decay rates from the first oscillations increase with the rise of OD, displaying a linear relationship with re-

spect to the OD. This dependence aligns well with the prediction of an enhanced decay rate in the superradiance emission interpretation as given as

$$\Gamma = \Gamma_0(1 + \alpha OD) . \quad (8)$$

The slope parameter α is fitted to be 0.15. The observation of two decay rates in different regimes indicates the existence of two distinct decay channels in the correlated photon pair mechanism: one decay rate close to the natural linewidth of the energy level and another enhanced decay rate, which not accounted for in the two-photon wave function as described in Eq.3.

VII. DETUNING DEPENDENCE

The detuning of the pump fields is a critical factor influencing the generation of correlated photon pairs from a nonlinear process. As shown in Fig.3 (a), approaching the atomic resonance of the pumping field does not intrinsically enhance the nonlinear process. Instead, the photon pair generation rates exhibit maximum at specific detunings on both positive and negative sides of the resonance. Specifically, the correlated photon pair rate is higher for positive detuning of the pumping field than negative detuning. This asymmetry results in a higher heralding efficiency in the Stokes channel for positive detuning. In contrast, the incoherent scattering photon rate follows a Lorentzian profile centered at the resonance.

Exploring the dependence on the coupling field detuning, Fig. 8 examines how the detuning of the coupling field Δ_c affects the correlated photon pair generation, while the pumping field is fixed to $\Delta_p = -50$ MHz. Within a detuning range from -40 MHz to 40 MHz, the correlated photon pair generation mechanism remains active, with the photon pair rate reaching its maximum at a specific negative detuning (around -25 MHz) rather than at the resonance. Excluding the Doppler broadening, which can be neglected in the counterpropagating pump configuration, the observed redshift and broadening in the photon pair rate may be attributed to the Lorentz-Lorenz shift [35, 36] or the collective Lamb shift in a dense medium [37–39]. Meanwhile, the waveform of $g_{as-s}^{(2)}(\tau)$ with large coupling field detuning exhibits distinct features compared to the scenario with a resonant coupling field. As illustrated in Fig. 9 (a), when the coupling field detuning Δ_c is set to -40 MHz, the heights of successive peaks become more pronounced, accompanied by a slower damped envelope. Furthermore, it is noted that the oscillations in the waveform do not extend to the background level of $g_{as-s}^{(2)} = 1$. This indicates that one frequency component in the Rabi splitting of the anti-Stokes mode dominates the four-wave mixing process rather than both frequencies exhibiting equal intensities in the case of the resonant coupling field. Our investigations into the detunings of the pumping field and coupling field reveal that correlated photon pairs can

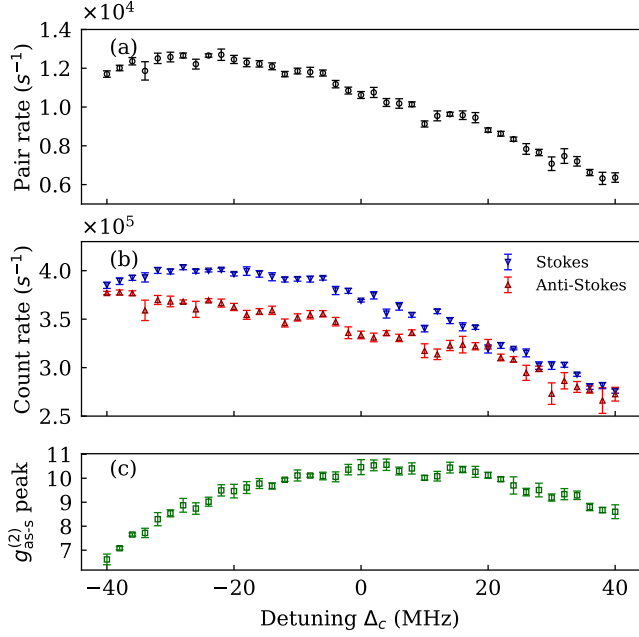


FIG. 8. (a)-(c) investigate the correlated photon pair rate, single count rate, and the peak of corrected $g_{\text{as-s}}^{(2)}$ as functions of the coupling field detuning Δ_c , with the constant pump field powers as $P_p \approx 700 \mu\text{W}$ and $P_c \approx 8.5 \text{ mW}$ and a fixed pumping detuning $\Delta_p = -50 \text{ MHz}$. The photon pair rate is determined by measuring the coincidence counts above the accidental background counts, without imposing a fixed coherence time. The similar trends in photon counts observed in both Stokes and anti-Stokes channels suggest that the frequency-dependent attenuation due to deviation from the center frequency of the anti-Stokes etalon can be considered negligible within this frequency range. The cross-correlation functions $g_{\text{as-s}}^{(2)}$ are only corrected by accounting for dark count rates of about 1300 s^{-1} for the Stokes channel and approximately 100 s^{-1} for the anti-Stokes channel.

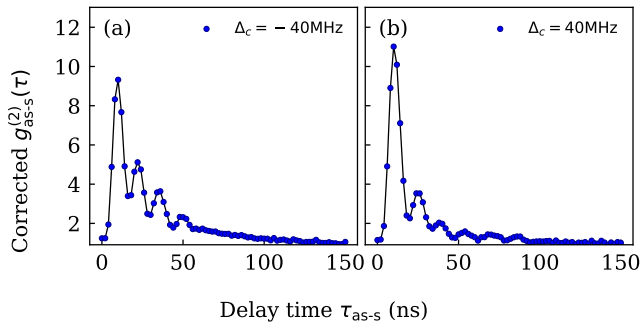


FIG. 9. Panel (a) depicts the waveform of the cross-correlation functions $g_{\text{as-s}}^{(2)}(\tau)$ at the coupling field detuning of $\Delta_c = -40 \text{ MHz}$, while (b) shows the waveform under $\Delta_c = 40 \text{ MHz}$. The experimental parameters remain consistent with the data in Fig. 8.

be generated efficiently over a relatively large detuning range in this double- Λ FWM nonlinear process.

VIII. CONCLUSION

In conclusion, we have successfully developed a bright correlated photon source in the paraxial regime of counter-propagating pump fields from a cold ^{87}Rb atomic ensemble. The correlated photon pairs are generated from a four-wave mixing parametric process based on the double- Λ energy scheme. This quantum source offers narrowband spectral characteristics and long coherence times, making it highly suitable for applications in atom-repeater quantum communication. The observed spectral properties, influenced predominantly by the coupling field intensity rather than the pump field intensity, highlight the role of linear susceptibility in determining bandwidth constraints. Although the dependence of spectral properties on the coupling field intensity shows a similar trend to the theoretical group-delay bandwidth, the predicted large group delay is not observed in the two-photon wave function, indicating experimental deviations from the previous theoretical models. Moreover, we also observe some features such as enhanced decay rate in the two-photon wave function and the dependence on OD, these properties suggest the involvement of the superradiance effects within the atomic ensemble for the generated photon pairs. To further validate the attributions of the superradiance in the nonlinear process and fully understand our observations, a comprehensive theoretical interpretation involving the collective effects of atomic emitters is necessary. This may help fully explain the behavior of this bright correlated photon pair source.

Appendix A: Instantaneous coincidence rate

The average correlated photon pair generation rate R_p is calculated from the total correlated photon pair number N_p detected over a measurement time T_m as follows:

$$R_p = \frac{N_p}{T_m} \quad (\text{A1})$$

From practical measurement counting, the measured pair detection rate is obtained from the coincidence counting between twin channels as

$$R_p^m = \frac{\sum_{n=0}^{n_c} N_c^m n \delta t}{T_m} \quad (\text{A2})$$

where n_c represents the number of coherence time bins, δt is the bin time, N_c denotes the number of coincidence counts above the background level within the time bin $n \delta t$ over a total measurement duration of T_m . Considering the total detection efficiencies η_1 for channel 1 and η_2 (including the transmission in the system and detection efficiencies of single-photon detectors), the measured pair

detection rate can be expressed as

$$R_p^m = \eta_1 \eta_2 R_p \quad (\text{A3})$$

Using the model for correlated photon pair generation from Ref.[1], the instantaneous coincidence rate $C(\tau)$ in one channel can also characterize the correlated photon source [1]. The quantity is linked to the measured correlated photon number as

$$N_c(\tau) = C(\tau)^2 \delta T_m. \quad (\text{A4})$$

Therefore, the normalized cross-correlation function $g^{(2)}(\tau)$ is expressed as [1]

$$g^{(2)}(\tau) = 1 + \frac{C^2(\tau)}{R_1 R_2}, \quad (\text{A5})$$

where R_1 and R_2 represent the single photon rate in twin channels, respectively. This indicates that the normalized cross-correlation function can be obtained by normalizing the coincidence counts between the twin channels against the average background counts in the far-coherence time regime. Accordingly, the measured instantaneous coincidence rate, $C^m(\tau)$ is given by

$$C^{(m)}(\tau) = \sqrt{\frac{M_c^m(\tau)}{\delta t T_m}}. \quad (\text{A6})$$

Appendix B: Coincidence histogram correction

In this four-wave mixing process, the rate of correlated photon pairs, denoted as R_2 , is proportional to the third-order susceptibility $\chi^{(3)}$. Concurrently, the linear susceptibility generates uncorrelated scattering photons in both Stokes and anti-Stokes modes, resulting in noise photon rates R_s^n and R_{as}^n respectively. In the experimental setup, these noise photon rates also account for the uncorrelated photons due to an imperfect collection

system. Therefore the total initial photon rate as

$$\begin{aligned} R_1 &= R_p + R_1^n \\ R_2 &= R_p + R_2^n. \end{aligned} \quad (\text{B1})$$

These photons are detected with probabilities (total detection efficiencies) η_1 and η_2 in the twin channels. These probabilities account for the total transmission ratio and detection efficiencies of the single-photon detectors. Additionally, accidental counts arise from laser leakage and dark counts of detectors, independent of the detection efficiencies, denoted as R_1^d for channel 1 and R_2^d for channel 2. Hence, the measured count rates R_1^m and R_2^m are given by

$$\begin{aligned} R_1^m &= R_p \eta_1 \eta_2 + R_p \eta_1 (1 - \eta_2) + R_1^n \eta_1 + R_1^d \\ R_2^m &= R_p \eta_1 \eta_2 + R_p \eta_2 (1 - \eta_1) + R_2^n \eta_2 + R_2^d. \end{aligned} \quad (\text{B2})$$

In the measurement of coincidence counting histogram, only terms $R_p \eta_1 \eta_2$ in two channels result in the coincidence peak above the background counts, corresponding to the measured correlated photon pairs. The mutual counts between other terms contribute to the background counts. Given that the normalized cross-correlation $g^{(2)}(\tau)$ is linked to the practical photon counting number via

$$\begin{aligned} g^{(2)}(\tau) &= 1 + \frac{C^2(\tau) \delta t T_m}{R_1 R_2 \delta t T_m} = 1 + \frac{\eta_1 \eta_2 C^2(\tau) \delta t T_m}{\eta_1 R_1^n \eta_2 R_2^n \delta t T_m} \\ &= 1 + \frac{N_p^m(\tau)}{N_{bg}} \end{aligned} \quad (\text{B3})$$

The valid background count per bin $N_{bg} = \eta_1 R_1^n \eta_2 R_2^n \delta t T_m$ forms a portion of the measured histogram background ($R_1^m R_2^m \delta t T_m$). Therefore, the coincidence histogram should be corrected by subtracting the following terms

- $R_1^d R_2^m \delta t T_m$
- $R_p \eta_1 (1 - \eta_2) R_2^m \delta t T_m$
- $R_1^n \eta_1 R_p \eta_2 + R_1^n \eta_1 R_2^d$
- $R_p^m (R_2 \eta_2 (1 - \eta_1) + R_2^n \eta_2 + R_2^d)$

After subtracting these terms from the coincidence histogram background, the residual background per bin corresponds to $R_1^n R_2^n \eta_1 \eta_2 \delta t T_m$.

-
- [1] C. H. Bennett and G. Brassard, Quantum cryptography: Public key distribution and coin tossing, *Theoretical Computer Science* **560**, 7 (2014).
 [2] F. Xu, X. Ma, Q. Zhang, H.-K. Lo, and J.-W. Pan, Secure quantum key distribution with realistic devices, *Reviews of Modern Physics* **92**, 025002 (2020).
 [3] P. Kok, W. J. Munro, K. Nemoto, T. C. Ralph, J. P. Dowling, and G. J. Milburn, Linear optical quantum

computing with photonic qubits, *Rev. Mod. Phys.* **79**, 135 (2007).

- [4] L. Pezzè, A. Smerzi, M. K. Oberthaler, R. Schmied, and P. Treutlein, Quantum metrology with nonclassical states of atomic ensembles, *Rev. Mod. Phys.* **90**, 035005 (2018).
 [5] C. Kurtsiefer, M. Oberparleiter, and H. Weinfurter, High-efficiency entangled photon pair collection in type-II parametric fluorescence, *Phys. Rev. A* **64**, 023802 (2001).

- [6] J. K. Thompson, J. Simon, H. Loh, and V. Vuletić, A high-brightness source of narrowband, identical-photon pairs, *Science* **313**, 74 (2006).
- [7] M. D. Lukin, A. B. Matsko, M. Fleischhauer, and M. O. Scully, Quantum Noise and Correlations in Resonantly Enhanced Wave Mixing Based on Atomic Coherence, *Physical Review Letters* **82**, 1847 (1999).
- [8] C. Shu, P. Chen, T. K. A. Chow, L. Zhu, Y. Xiao, M. Loy, and S. Du, Subnatural-linewidth biphotons from a Doppler-broadened hot atomic vapour cell, *Nature Communications* **7**, 12783 (2016).
- [9] J. Park, T. Jeong, and H. S. Moon, Spectral-temporal biphoton waveform of photon pairs from cascade-type warm atoms, *Scientific Reports* **10**, 16413 (2020).
- [10] A. Kuzmich, W. P. Bowen, A. D. Boozer, A. Boca, C. W. Chou, L.-M. Duan, and H. J. Kimble, Generation of non-classical photon pairs for scalable quantum communication with atomic ensembles, *Nature* **423**, 731 (2003).
- [11] P. Kolchin, S. Du, C. Belthangady, G. Y. Yin, and S. E. Harris, Generation of Narrow-Bandwidth Paired Photons: Use of a Single Driving Laser, *Physical Review Letters* **97**, 113602 (2006).
- [12] B. Srivathsan, G. K. Gulati, C. M. Y. Brenda, G. Maslennikov, D. Matsukevich, and C. Kurtsiefer, Narrow Band Source of Transform-Limited Photon Pairs via Four-Wave Mixing in a Cold Atomic Ensemble, *Physical Review Letters* **111**, 123602 (2013).
- [13] S. Du, P. Kolchin, C. Belthangady, G. Y. Yin, and S. E. Harris, Subnatural Linewidth Biphotons with Controllable Temporal Length, *Physical Review Letters* **100**, 183603 (2008).
- [14] S. Du, J. Wen, and C. Belthangady, Temporally shaping biphoton wave packets with periodically modulated driving fields, *Physical Review A* **79**, 043811 (2009).
- [15] L. Zhao, X. Guo, Y. Sun, Y. Su, M. M. T. Loy, and S. Du, Shaping the Biphoton Temporal Waveform with Spatial Light Modulation, *Physical Review Letters* **115**, 193601 (2015).
- [16] G. K. Gulati, B. Srivathsan, B. Chng, A. Cerè, and C. Kurtsiefer, Polarization entanglement and quantum beats of photon pairs from four-wave mixing in a cold ^{87}Rb ensemble, *New Journal of Physics* **17**, 093034 (2015).
- [17] A. Cerè, B. Srivathsan, G. K. Gulati, B. Chng, and C. Kurtsiefer, Characterization of a photon-pair source based on a cold atomic ensemble using a cascade-level scheme, *Physical Review A* **98**, 023835 (2018).
- [18] V. Balić, D. A. Braje, P. Kolchin, G. Y. Yin, and S. E. Harris, Generation of Paired Photons with Controllable Waveforms, *Physical Review Letters* **94**, 183601 (2005).
- [19] J. Wen, S. Du, and M. H. Rubin, Biphoton generation in a two-level atomic ensemble, *Physical Review A* **75**, 033809 (2007).
- [20] S. Du, J. Wen, and M. H. Rubin, Narrowband biphoton generation near atomic resonance, *J. Opt. Soc. Am. B* **25**, C98 (2008).
- [21] S. E. Harris, J. E. Field, and A. Imamoglu, Nonlinear optical processes using electromagnetically induced transparency, *Phys. Rev. Lett.* **64**, 1107 (1990).
- [22] L. Zhao, X. Guo, C. Liu, Y. Sun, M. M. T. Loy, and S. Du, Photon pairs with coherence time exceeding $1\ \mu\text{s}$, *Optica* **1**, 84 (2014).
- [23] C. H. Raymond Ooi, Q. Sun, M. S. Zubairy, and M. O. Scully, Correlation of photon pairs from the double Raman amplifier: Generalized analytical quantum Langevin theory, *Physical Review A* **75**, 013820 (2007).
- [24] P. Kolchin, Electromagnetically-induced-transparency-based paired photon generation, *Physical Review A* **75**, 033814 (2007).
- [25] Y. Jiang, Y. Mei, and S. Du, Quantum Langevin theory for two coupled phase-conjugated electromagnetic waves, *Physical Review A* **107**, 053703 (2023).
- [26] L. Zhao, Y. Su, and S. Du, Narrowband biphoton generation in the group delay regime, *Physical Review A* **93**, 033815 (2016).
- [27] Y. Mei, Y. Zhou, S. Zhang, J. Li, K. Liao, H. Yan, S.-L. Zhu, and S. Du, Einstein-Podolsky-Rosen Energy-Time Entanglement of Narrow-Band Biphotons, *Physical Review Letters* **124**, 010509 (2020).
- [28] J.-S. Shiu, Z.-Y. Liu, C.-Y. Cheng, Y.-C. Huang, I. A. Yu, Y.-C. Chen, C.-S. Chuu, C.-M. Li, S.-Y. Wang, and Y.-F. Chen, Observation of highly correlated ultrabright biphotons through increased atomic ensemble density in spontaneous four-wave mixing (2023), 2312.12758.
- [29] R. H. Dicke, Coherence in Spontaneous Radiation Processes, *Physical Review* **93**, 99 (1954).
- [30] P. Grivet, N. Bloembergen, and U. S. O. of Naval Research, *Quantum Electronics: Proceedings of the Third International Congress*, Quantum Electronics: Proceedings of the Third International Congress No. v. 1 (Dunod, 1964).
- [31] L.-M. Duan, M. D. Lukin, J. I. Cirac, and P. Zoller, Long-distance quantum communication with atomic ensembles and linear optics, *Nature* **414**, 413 (2001).
- [32] T. Chanelière, D. N. Matsukevich, S. D. Jenkins, T. A. B. Kennedy, M. S. Chapman, and A. Kuzmich, Quantum Telecommunication Based on Atomic Cascade Transitions, *Physical Review Letters* **96**, 093604 (2006).
- [33] H. H. Jen, Positive- P phase-space-method simulation of superradiant emission from a cascade atomic ensemble, *Physical Review A* **85**, 013835 (2012).
- [34] H. Jen, Superradiant cascade emissions in an atomic ensemble via four-wave mixing, *Annals of Physics* **360**, 556 (2015).
- [35] S. E. Schnatterly and C. Tarrío, Local fields in solids: microscopic aspects for dielectrics, *Rev. Mod. Phys.* **64**, 619 (1992).
- [36] J. Javanainen and J. Ruostekoski, Light propagation beyond the mean-field theory of standard optics, *Opt. Express* **24**, 993 (2016).
- [37] M. O. Scully, Collective lamb shift in single photon dicke superradiance, *Physical Review Letters* **102**, 143601 (2009).
- [38] J. Keaveney, A. Sargsyan, U. Krohn, I. G. Hughes, D. Sarkisyan, and C. S. Adams, Cooperative lamb shift in an atomic vapor layer of nanometer thickness, *Physical Review Letters* **108**, 173601 (2012).
- [39] S. J. Roof, K. J. Kemp, M. D. Havey, and I. M. Sokolov, Observation of single-photon superradiance and the cooperative lamb shift in an extended sample of cold atoms, *Physical Review Letters* **117**, 073003 (2016).